Supplementary Information (SI) for Materials Horizons.
This journal is © The Royal Society of Chemistry 2024

Supporting Information

Outstanding High-Temperatures Capacitive Performance in All-Organic Dielectrics Enabled by Synergistic Optimization of Molecular Trap and Aggregation Structure

Bo Peng,[a] Pengbo Wang,[b] Hang Luo,*[a] Guanghu He,[a] Haoran Xie,[a] Yuan Liu,[a] Sheng Chen,[c] Xiaona Li,[a] Yuting Wan [a] and Ru Guo *[a]

[a] Powder Metallurgy Research Institute, State Key Laboratory of Powder Metallurgy, Central South University, Changsha, Hunan, 410083, China.
E-mail address: hangluo@csu.edu.cn (Hang Luo).
[b] b. Department of Chemical and Biological Engineering, The Hong Kong University of Science and Technology, Hong Kong, 999077, China.
[c] Key Laboratory of Polymeric Materials and Application Technology of Hunan Province, College of Chemistry, Xiangtan University, Xiangtan, Hunan, 411105, China.
[d] Department of Mechanical and Automation Engineering, The Chinese University of Hong Kong, Shatin, N.T. Hong Kong, 999077, China

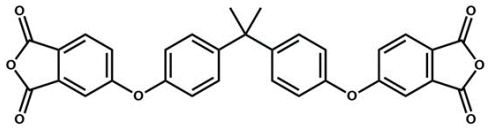

BPADA

4,4'-(4,4'-Isopropylidenediphenoxy)diphthalic Anhydride

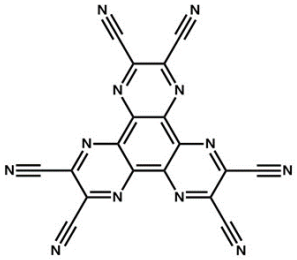

HAT-CN

Dipyrazino[2,3-f:2′,3′-h]quinoxaline-2,3,6,7,10,11-hexacarbonitrile

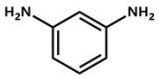

MPD

m-Phenylenediamine

Fig. S1 Chemical structures of the BPADA, MPD and HAT-CN.

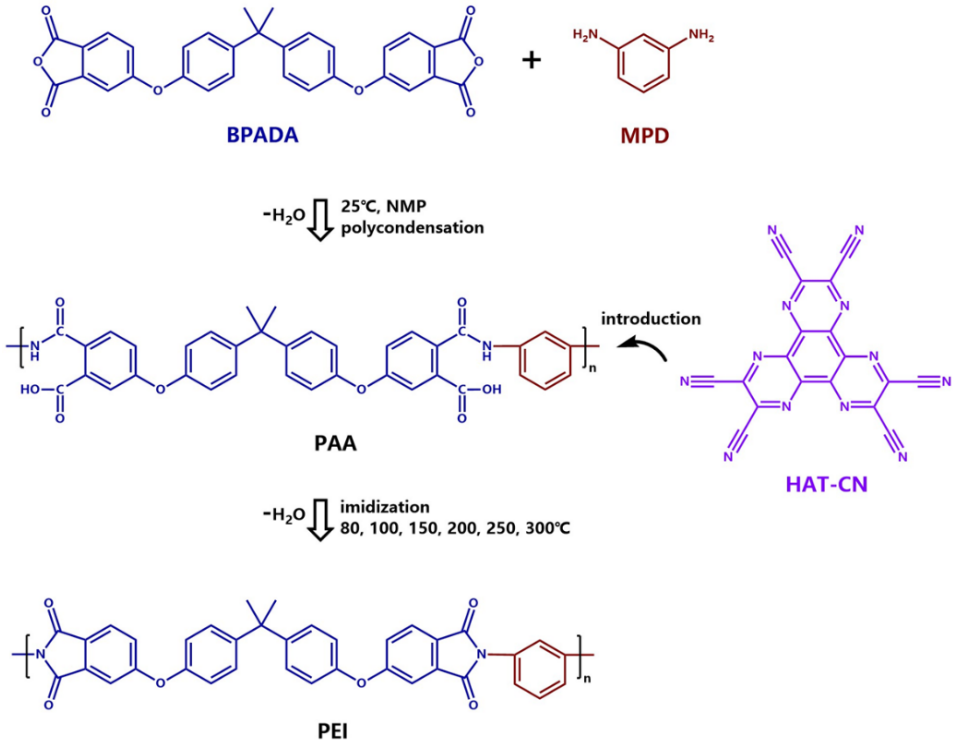

Fig. S2 Chemical process diagram for preparation of HAT-CN/PEI all-organic composite films.

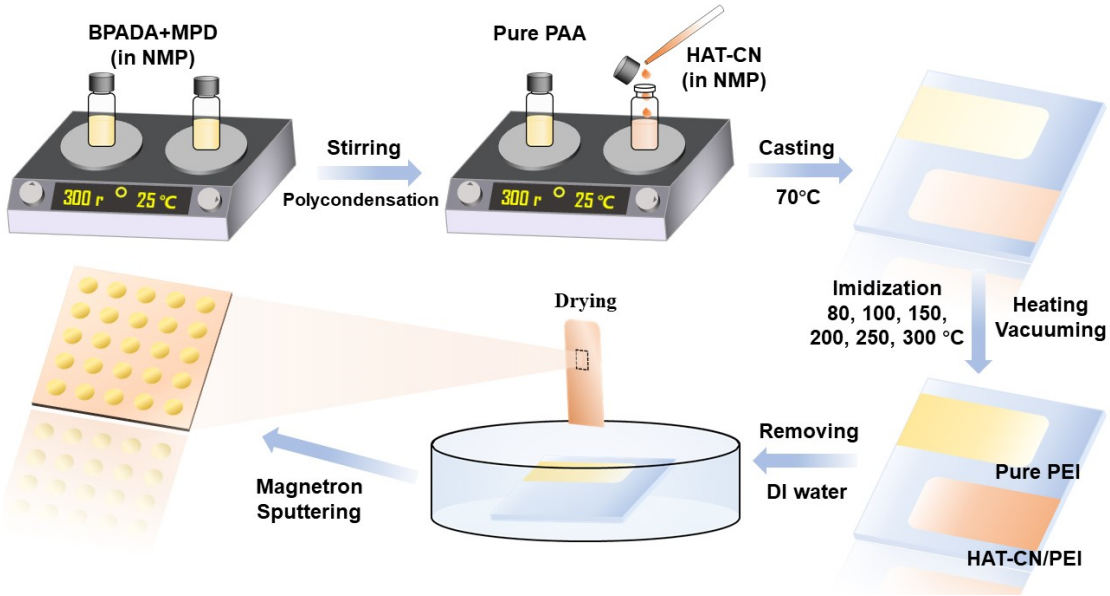

Fig. S3 Experimental process diagram for preparation of HAT-CN/PEI all-organic composite films.

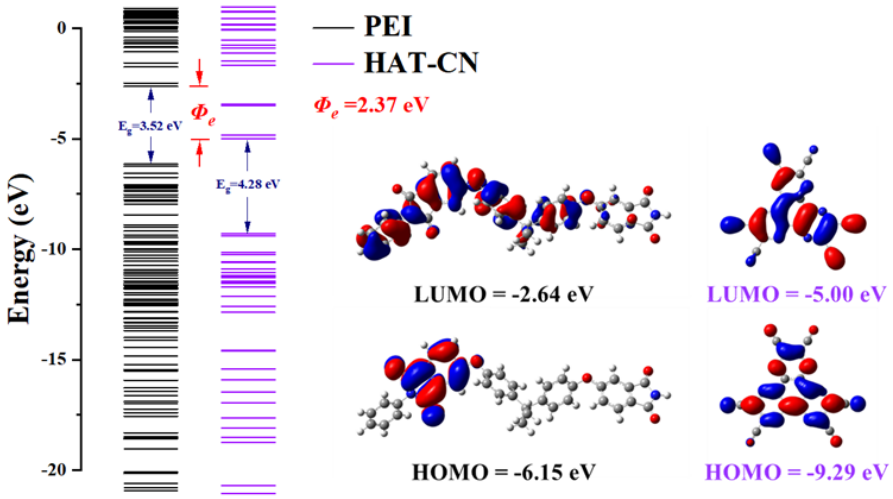

Fig. S4 The band structure of PEI and HAT-CN were simulated by DFT calculation. PEI is located on the left side, while HAT-CN is located on the right side.

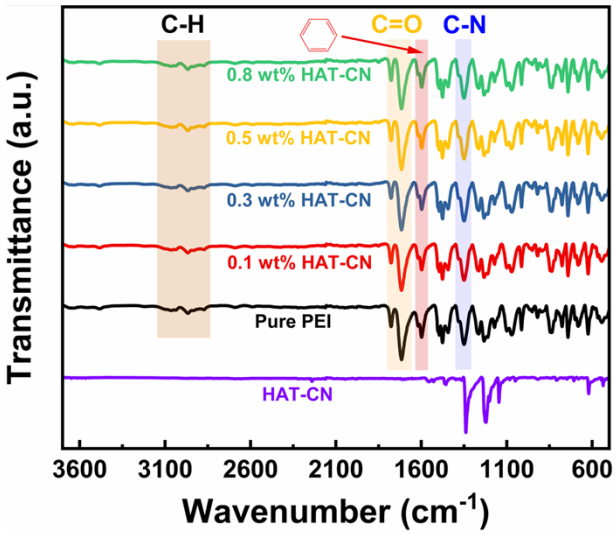

Fig. S5 The FTIR spectra of HAT-CN and the composite films loaded with different content of HAT-CN.

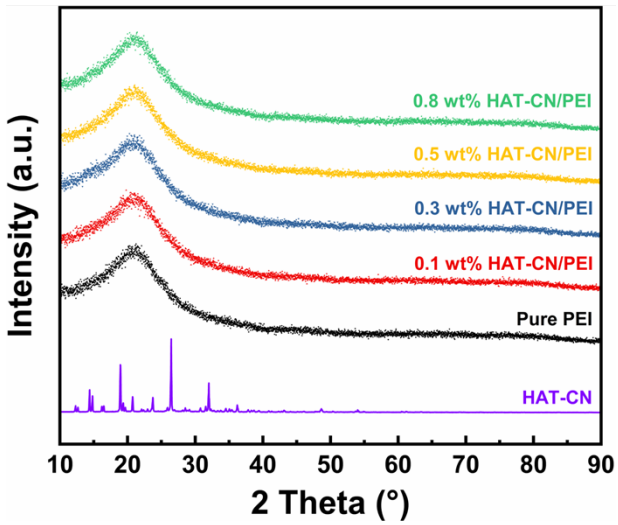

Fig. S6 The XRD patterns of HAT-CN and the composite films loaded with different content of HAT-CN.

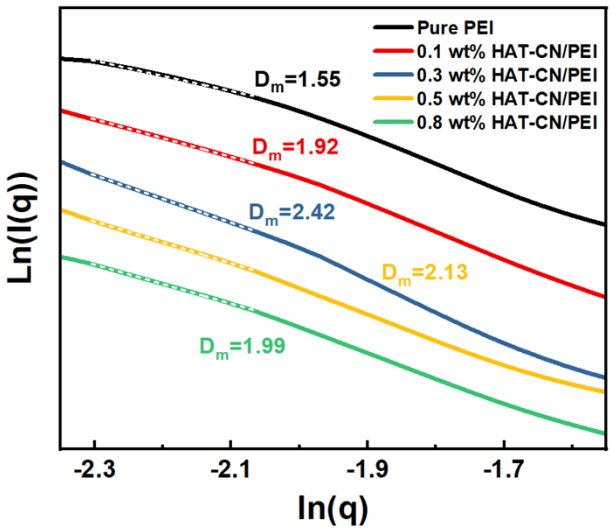

Fig. S7 The SAXS curves of the composite films loaded with different content of HAT-CN.

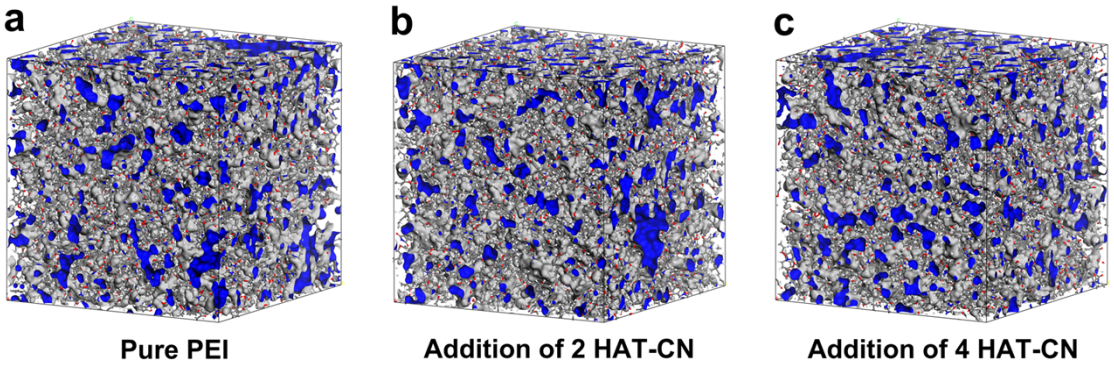

Fig. S8 Simulated snapshots of a) PEI and b,c,d) HAT-CN/PEI composites in molecular dynamics simulation.

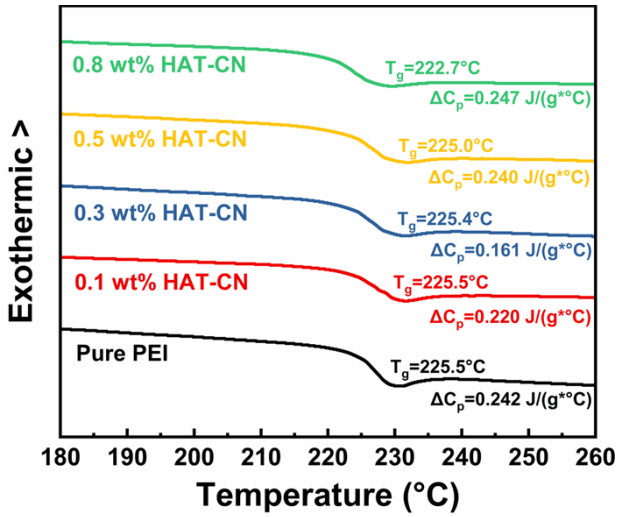

Fig. S9 The DSC curves of the composite films loaded with different content of HAT-CN.

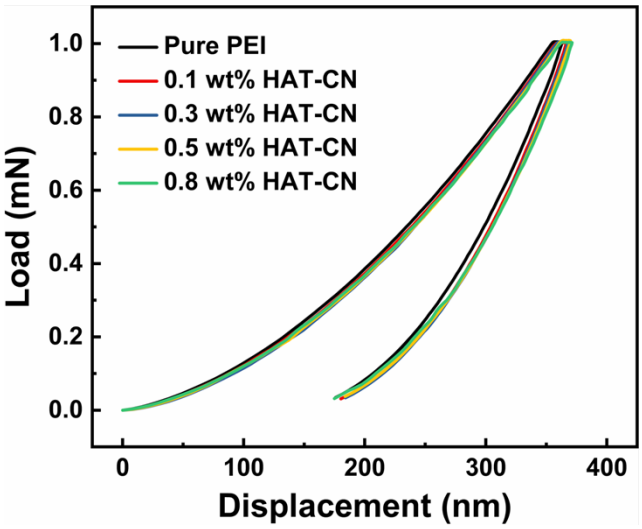

Fig. S10 The load-displacement curves of the composite films loaded with different content of HAT-CN.

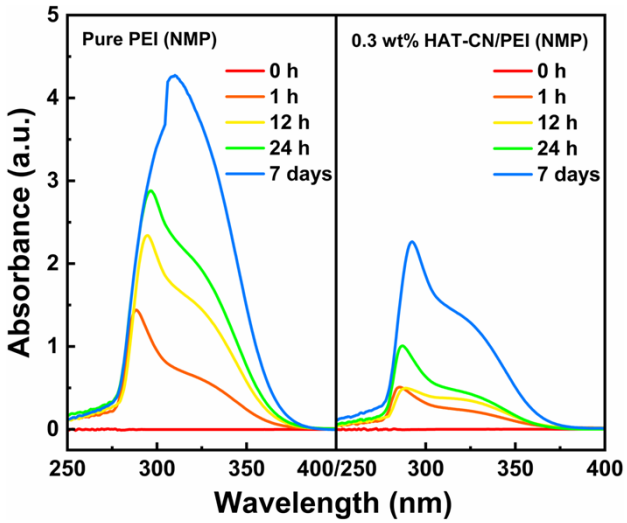

Fig. S11 The UV-vis absorption spectra of PEI and 0.3 wt% HAT-CN/PEI dissolved in NMP, which are used to determine the difference in solubility of them.

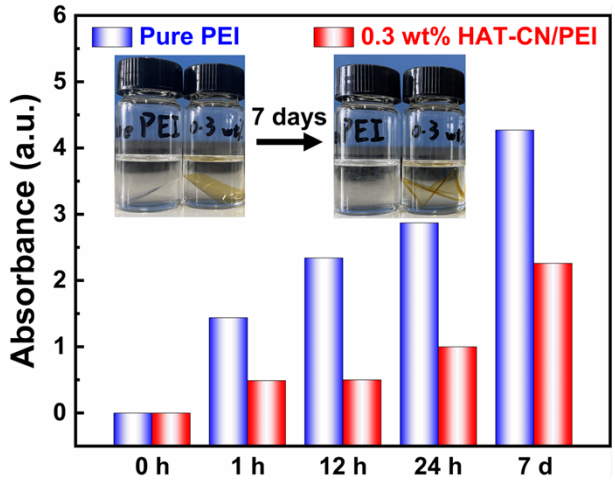

Fig. S12 The solubility of the films in NMP at different time which studied by UV-vis spectra. The ordinate of the bar chart is taken from the highest value of the peak of UV-vis absorption spectra of the samples.

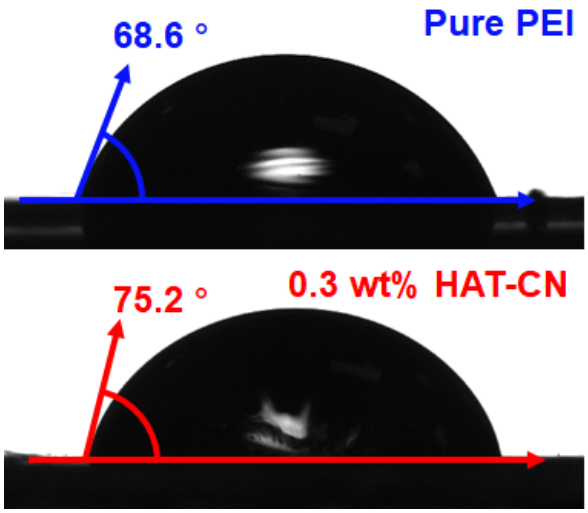

Fig. S13 The contact angles of PEI and 0.3 wt% HAT-CN/PEI determined by water solvent.

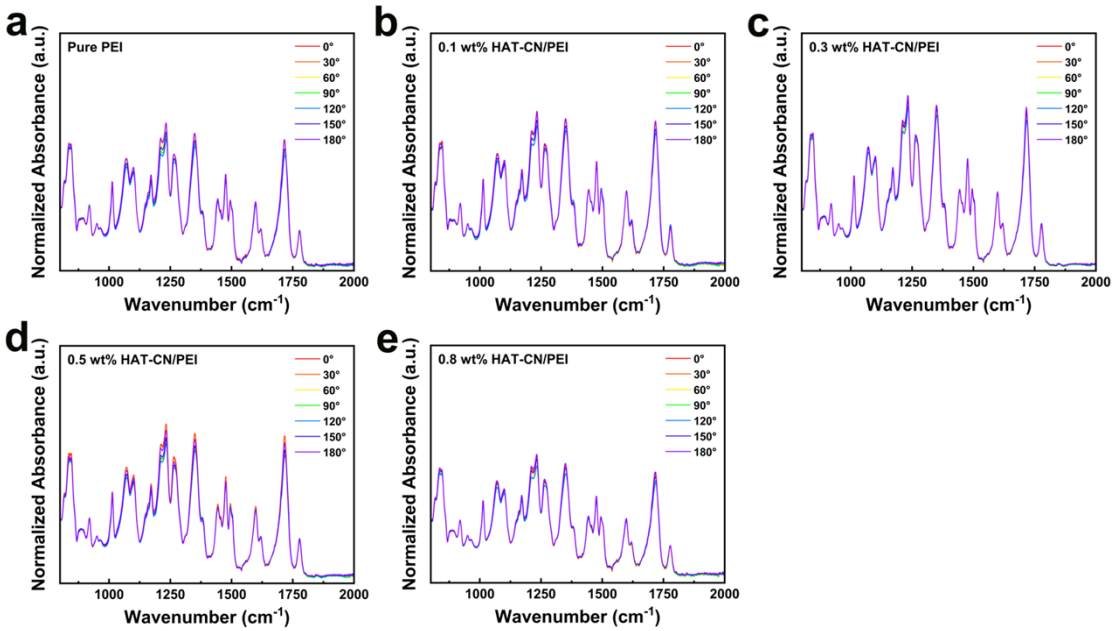

Fig. S14 Polarized FTIR spectra of the composite films loaded with different content of HAT-CN.

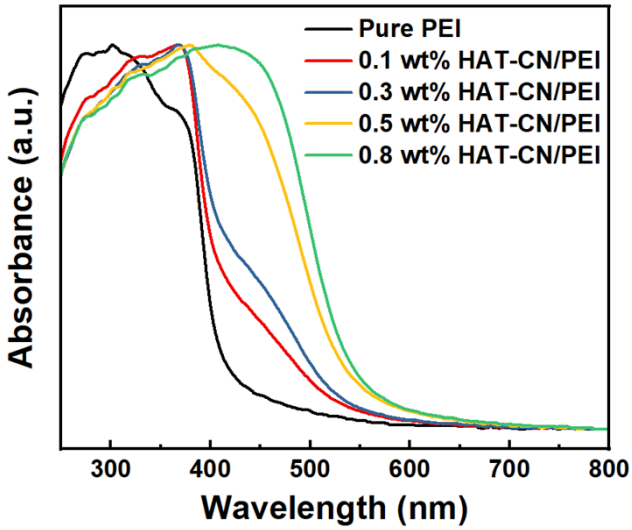

Fig. S15 UV-vis absorption spectra of all the composite films loaded with different content of HAT-CN.

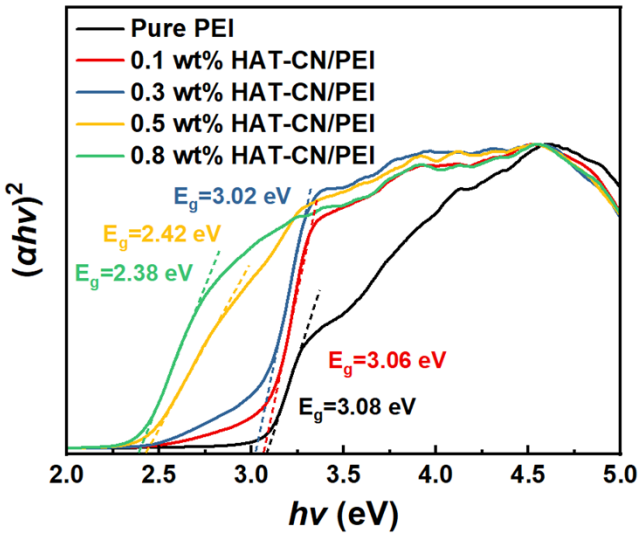

Fig. S16 The $(\alpha hv)^2$ – hv plots of the films, which were converted from the UV-vis absorption spectra by Tauc plot, in which α, h, and v are the absorption coefficient, Planck constant, and light frequency, respectively.

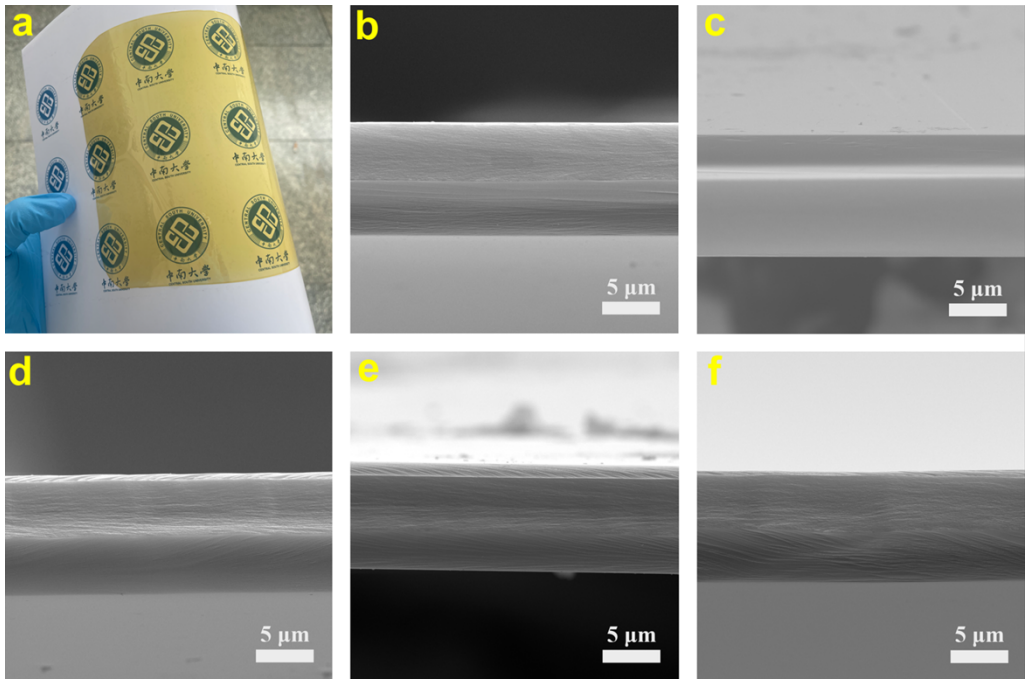

Fig. S17 a) Photos of 0.3 wt% HAT-CN/PEI film with dimensions of 15 cm × 15 cm, showing its flexibility. Cross-sectional SEM images of b) PEI, c) 0.1 wt% HAT-CN/PEI, d) 0.3 wt% HAT-CN/PEI, e) 0.5 wt% HAT-CN/PEI, and f) 0.8 wt% HAT-CN/PEI. The polymer films whose thickness ranging from 9 to 10 μm

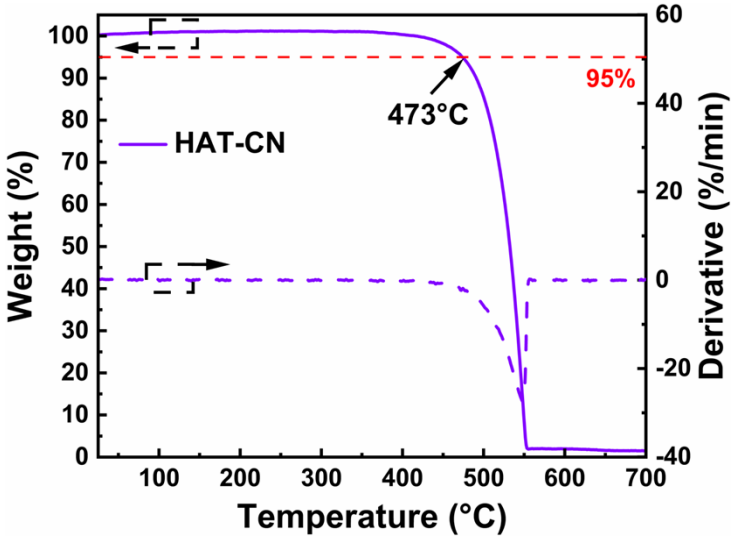

Fig. S18 The TGA curves of HAT-CN. It is shown that HAT-CN can maintain excellent thermal stability till 400 °C, so as to ensure that no reaction occurs during imidization.

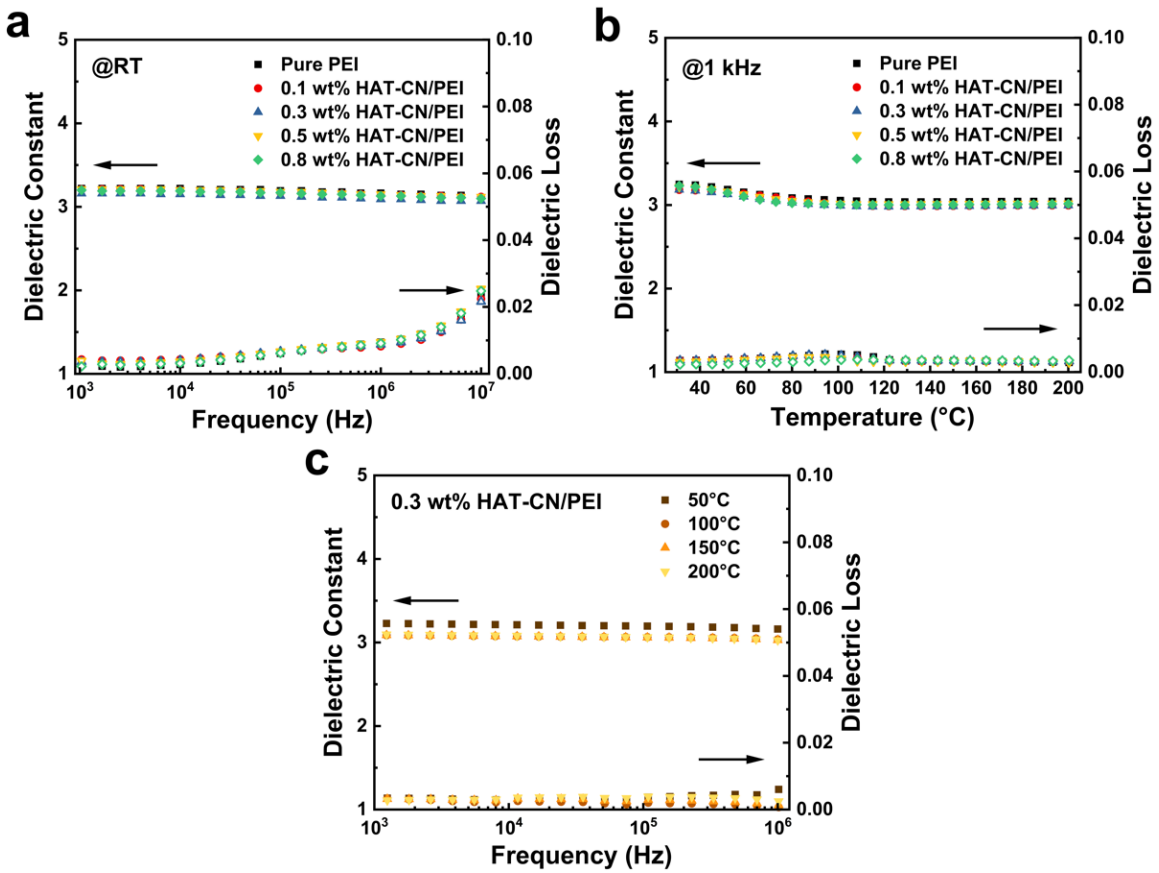

Fig. S19 a) Frequency dependence of ε_r and D of all samples at room temperatures. b) Temperature dependence of ε_r and D of all samples at 1 kHz. c) Frequency dependence of ε_r and D of 0.3 wt% HAT-CN/PEI composite film at different temperatures.

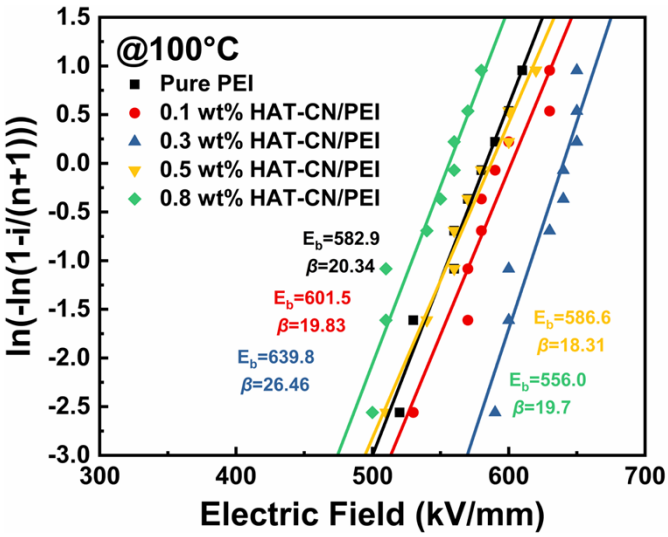

Fig. S20 The Weibull statistic of E_b of the samples with increasing electric field at 100 °C.

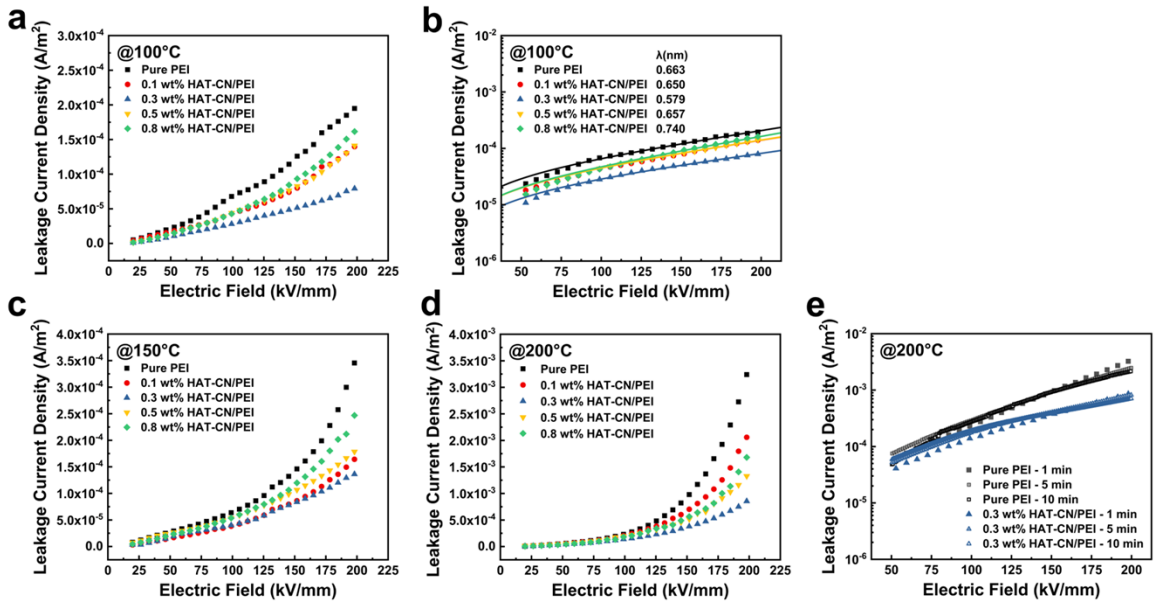

Fig. S21 Leakage current density of the samples with increasing electric field at a) 100°C, c) 150°C and d) 200°C. b) The hopping distance of the samples at 100 °C. e) Leakage current density of Pure PEI and 0.3 wt% HAT-CN/PEI under different test times at 200°C

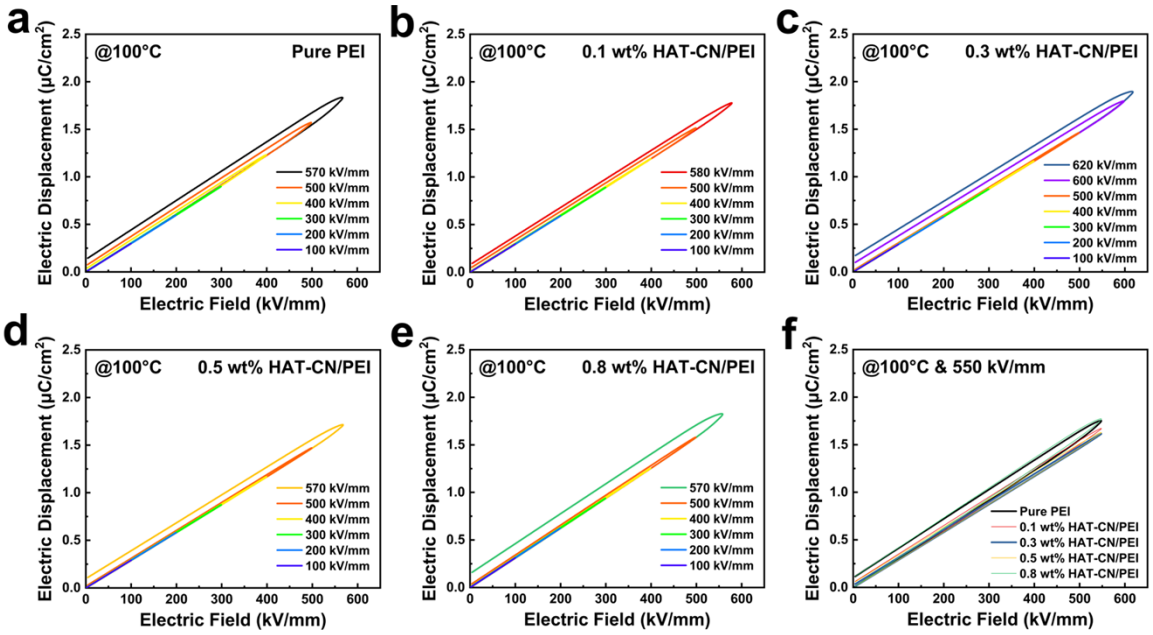

Fig. S22 The *D-E* loops of a) PEI, b) 0.1 wt% HAT-CN/PEI, c) 0.3 wt% HAT-CN/PEI, d) 0.5 wt% HAT-CN/PEI, e) 0.8 wt% HAT-CN/PEI and f) all the samples at 100 °C and 550 kV mm^{-1}.

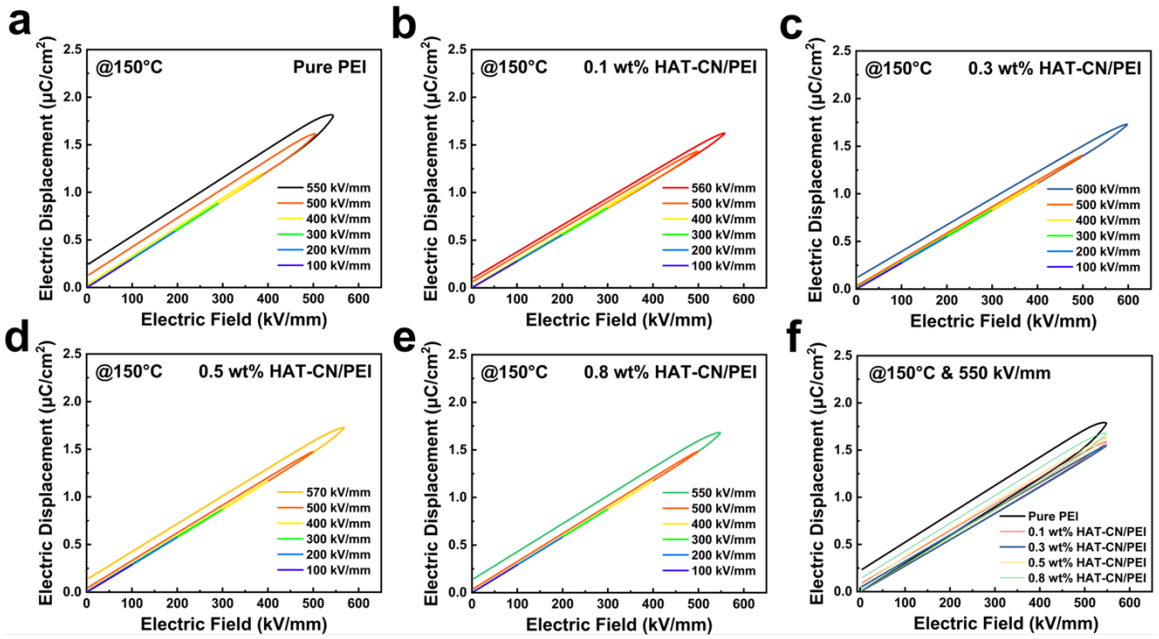

Fig. S23 The *D-E* loops of a) PEI, b) 0.1 wt% HAT-CN/PEI, c) 0.3 wt% HAT-CN/PEI, d) 0.5 wt% HAT-CN/PEI, e) 0.8 wt% HAT-CN/PEI and f) all the samples at 150 °C and 550 kV mm^{-1}.

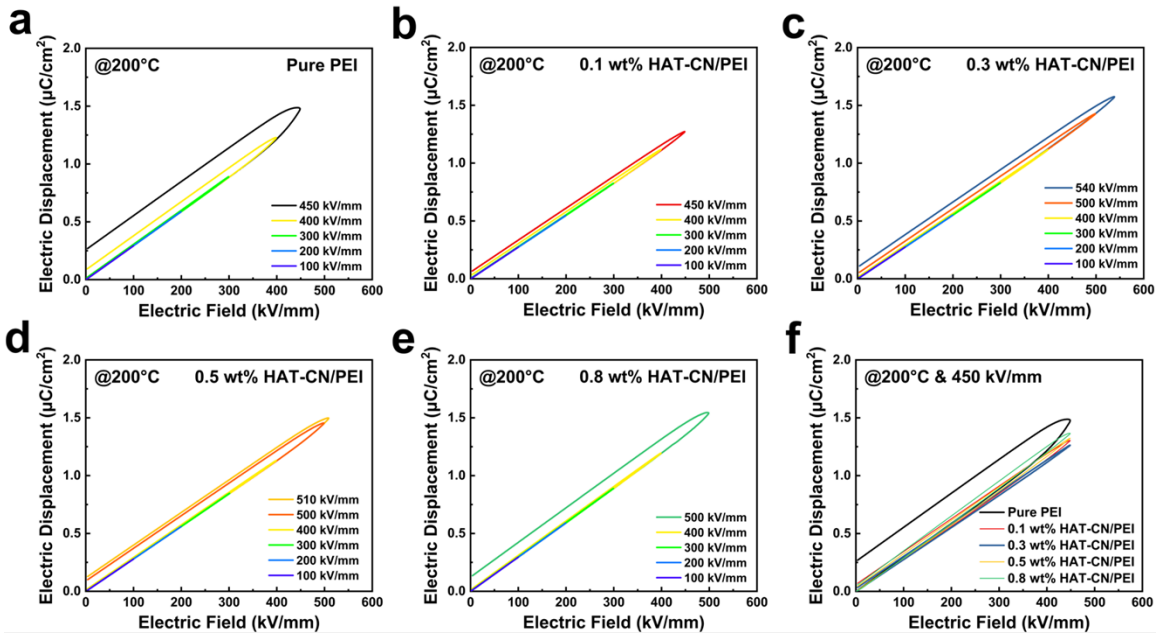

Fig. S24 The *D*-*E* loops of a) PEI, b) 0.1 wt% HAT-CN/PEI, c) 0.3 wt% HAT-CN/PEI, d) 0.5 wt% HAT-CN/PEI, e) 0.8 wt% HAT-CN/PEI and f) all the samples at 200 °C and 450 kV mm^{-1}.

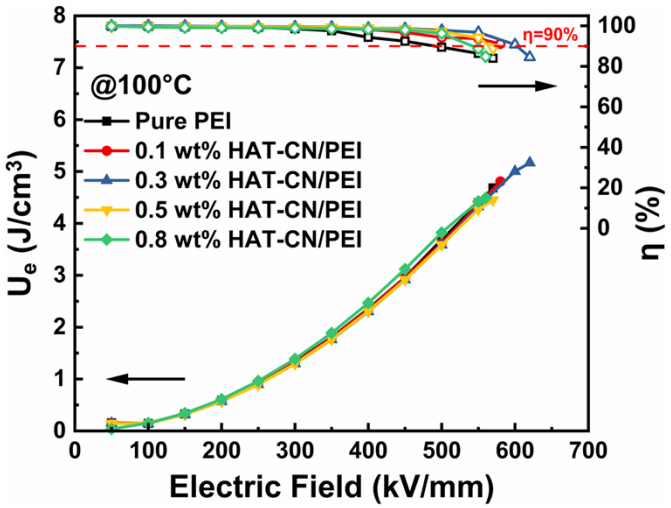

Fig. S25 U_e and η of the films at 100 °C.

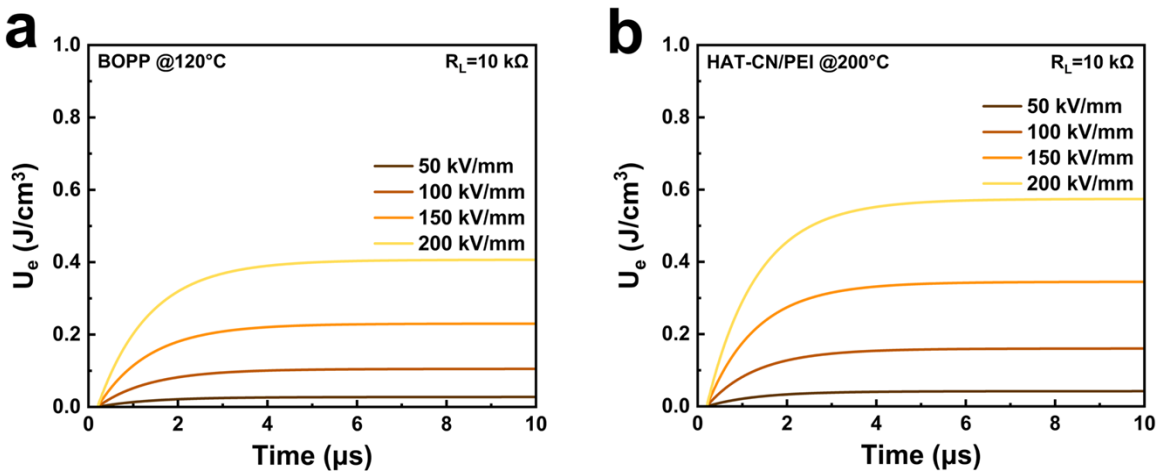

Fig. S26 Time dependence of U_e under different electric fields of a) BOPP and b) 0.3 wt% HAT-CN/PEI.

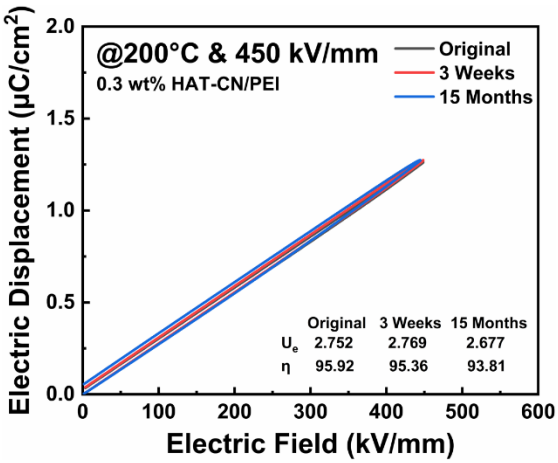

Fig. S27 The *D-E* loops of the composite film (Original, After 3 weeks and 15 months) at 200 °C & 450 kV mm^{-1}.